THE JOURNAL OF PHYSICAL CHEMISTRY C

Article

Cite This: J. Phys. Chem. C 2019, 123, 2557−2564

pubs.acs.org/JPCC

Shape and Surface Charge Modulation of Topological Domains in Oxide Multiferroics

Meng-Jiao Han,[†,‡,⊥] Yu-Jia Wang,[†,⊥] Yun-Long Tang,[†] Yin-Lian Zhu,[*,†] Jin-Yuan Ma,[†,§,∥] Wan-Rong Geng,[†,§] Min-Jie Zou,[†,§] Yan-Peng Feng,[†,‡] Ning-Bin Zhang,[†,§] and Xiu-Liang Ma[*,†,∥]

[†]Shenyang National Laboratory for Materials Science, Institute of Metal Research, Chinese Academy of Sciences, Wenhua Road 72, 110016 Shenyang, China

[‡]Center of Materials Science and Optoelectronics Engineering, University of Chinese Academy of Sciences, Yuquan Road 19, 100049 Beijing, China

[§]University of Science and Technology of China, Jinzhai Road 96, 230026 Hefei, China

[∥]State Key Lab of Advanced Processing and Recycling on Non-ferrous Metals, Lanzhou University of Technology, Langongping Road 287, 730050 Lanzhou, China

Supporting Information

ABSTRACT: Topological defects showing exotic properties and diverse functionalities provide us a potential utilization in nanoscale electronic devices. However, the formation mechanism and density manipulation of topological defects such as center-type domains which are crucial for applications remain elusive. Usually, these center-type domains are generated by applying external electric fields in ferroelectrics. In contrast, here we have prepared high-density center-divergent domains in $BiFeO_3$ as self-assembled nanoislands deposited on both Nb- and Fe-doped $SrTiO_3$ substrates. The size and density of these domains can be easily manipulated by varying doping level in substrates. The panorama polar configurations of the center-divergent domains are revealed by piezoresponse force microscopy and Cs-corrected scanning transmission electron microscopy. Phase-field simulations prove that both the surface charge accumulation and the shape of the nanoislands take great effect in the formation of center-type domains. The controllable growth of the nanoislands offers us a promising way to acquire high-density nanoscale nonvolatile memories.

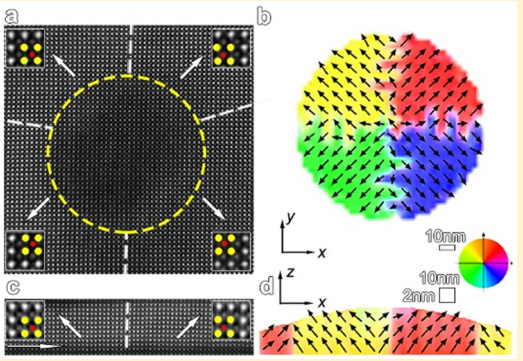

1. INTRODUCTION

Topological defects[1] in ferroelectric materials are of increasing interest due to their novel functionalities and potential applications in nonvolatile memories. "Topological defect" is a concept in the field of condensed matter physics which refers to a region where the order parameter varies discontinuously.[1,2] Those regions include points, lines, and surfaces such as screw dislocations, domain walls, vortices, skyrmions, and other domain structure defects. Ferroelectric topological domain arrangements arouse much attention since the dimension of dipole domain walls is much smaller than the magnetic ones, in which the ferroelectric vortex is a typical example. A vortex polarization pattern was early predicted in $BaTiO_3$ colloidal quantum dots[3] and $Pb(Zr,Ti)O_3$ nanoscale disks[4] and was experimentally observed in $PbZr_{0.2}Ti_{0.8}O_3$ capacitors during the reversal of polarization[5] and $Pb(Zr,Ti)O_3$ nanodots.[6] Electric fields produced by the external bias applied to the scanning probe microscope tip also can be the driving force for the formation of various topological domains including closure domains.[7,8] An obvious enhanced conductivity at the artificially created ferroelectric vortices has also been reported.[9] Another intriguing breakthrough is the discovery of periodical flux-closure domains[10] and vortices[11] in $PbTiO_3/SrTiO_3$ multilayers and superlattices, where the evolution of topological domain structures and the control of vortex chirality in nanodots by homogeneous electric field are investigated.[12−15]

In addition, another field of great interest is the search for stable exotic topological ferroelectric domains and study of related functionalities. A series of exotic topological defects have been discovered, including center domains,[8,16,17] bubble domains,[18] hedgehog polarization states,[19] dipole waves, and dipole disclinations.[20] Being another topological defect holding great promise for memories with ultrahigh densities, center-type domain has attracted a lot of interest in recent years. Usually, center-type domains are generated during polarization switching when external electric fields are applied in ferroelectrics.[8,16] Recently, high-density arrays of reversible center-type domains are found to be formed in nanodots fabricated using nanoporous anodic alumina template.[17] The formation

Received: November 1, 2018
Revised: December 30, 2018
Published: January 15, 2019

DOI: 10.1021/acs.jpcc.8b10678
J. Phys. Chem. C 2019, 123, 2557−2564

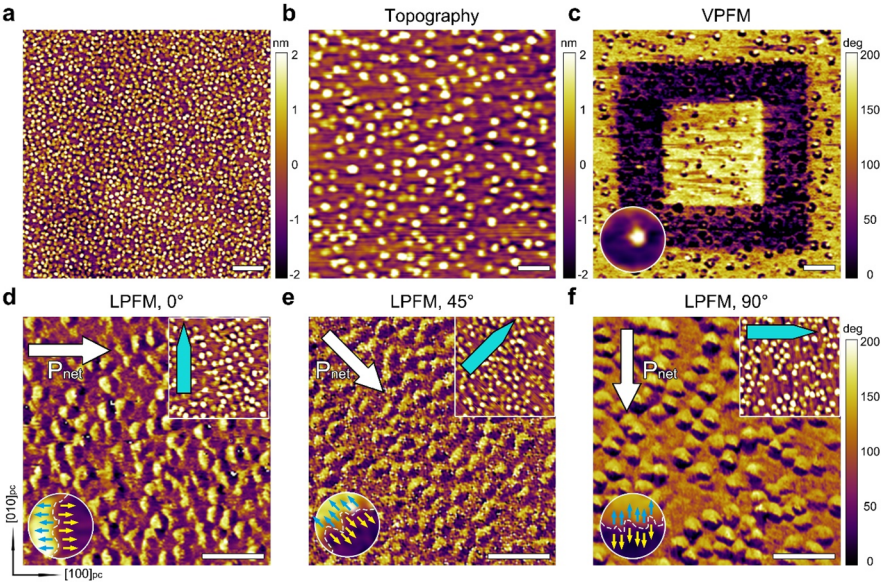

Figure 1. PFM analyses of BFO nanoislands on NSTO substrate. (a) Topography of 6 nm BFO deposited on NSTO (0.7 wt %) substrate. Scale bar, 1 μm. Topography (b) and corresponding VPFM (c) images of BFO nanoislands after writing an area of 3 × 3 μm^2 with a voltage of −10 V and then the inside 1.6 × 1.6 μm^2 with a voltage of +15 V. (d)−(f) LPFM images with anticlockwise sample rotation for 0° (d), 45° (e), and 90° (f) of these nanoislands. The net polarization detected is shown as the white arrow in each image. Upper right insets in (d)−(f) are topographies of the images. The cantilever direction in each case is also shown as the large blue arrow. Lower left insets in (c)−(f) are enlarged images of single nanoisland in each. All scale bars in (b)−(f) indicate 500 nm.

mechanism of various types of center domains was ascribed to different compensating charges on the surface. Moreover, Ma et al.[21] acquired self-assembled center-type domains and discovered a controllable conductive readout in the domain walls which is beneficial for future applications. However, the research of center-type domains is still at the starting point; especially, the polarization distribution of center-type domains at atomic scale is still lacking. Besides, the formation mechanism of center-type domains and its manipulation are also in need of in-depth investigation.

We successfully obtained high-density self-assembled $BiFeO_3$ (BFO) nanoislands which were deposited on Nb:$SrTiO_3$ (NSTO) and Fe:$SrTiO_3$ (FSTO) substrates through the adjustment of deposition conditions using pulsed laser deposition (PLD) method. By using the piezoresponse force microscopy (PFM) and transmission electron microscopy (TEM) measurements, a four-quadrant center-divergent domain structure separated by 71° zigzag-like charged domain walls was clearly revealed in these nanoislands. Phase-field simulations prove that both the surface charge accumulation and the shape of the nanoislands take great effect in the formation of the topological domain structure. Moreover, the size and density of these nanoislands can be adjusted by the thickness of the film and doping amount in substrates, which is of great benefit for high-density electronic devices.

2. METHODS

2.1. Material Preparation. BFO films were deposited by PLD, using a Coherent ComPex PRO 201 F KrF (λ = 248 nm) excimer laser. A sintered stoichiometric BFO ceramic target was used. The target−substrate distance was 32 mm. Before deposition, the substrates were heated up to 850 °C for 20 min to clean the surface. A substrate temperature of 800 °C, an oxygen pressure of 12 Pa, a repetition rate of 10 Hz, and a laser energy density of 2 $J \cdot cm^{-2}$ were applied during deposition. After deposition, these samples were kept at 800 °C for 5 min and then cooled down to room temperature at a cooling rate of 5 $°C \cdot min^{-1}$ in an oxygen pressure of 3 × 10^4 Pa. Commercial, one-side polishing Nb:$SrTiO_3$ (0.1 wt %) (001), Nb:$SrTiO_3$ (0.7 wt %) (001), Fe:$SrTiO_3$ (0.005 wt %) (001), and Fe:$SrTiO_3$ (0.05 wt %) (001) single-crystal substrates with 10 mm × 10 mm × 0.5 mm dimension were used for film deposition.

2.2. Piezoresponse Force Microscopy. The local piezoresponse was carried out by PFM on a commercial AFM system (Cypher, Asylum Research) in ambient conditions at room temperature. The probes used were Ti/Ir (5/20) coated tips (ASYELEC-01-R) with nominal k = 2.8 $N \cdot m^{-1}$. The contact frequencies for vertical PFM (VPFM) and lateral PFM (LPFM) measurements are set around 350 and 760 kHz for each. A Dual AC Resonance Tracking (DART) mode is used throughout the PFM measurements to reduce the topographic characteristics interference in the VPFM and LPFM images.

2.3. TEM and HAADF-STEM Imaging. Specimens for the TEM and HAADF-STEM experiments were prepared by traditional method: slicing, gluing, grinding, dimpling, and ion milling. A Gatan 691 PIPS was used for the final ion milling. To reduce the ion beam damage, the final ion milling voltage was <1 kV. TEM experiments and EDS mappings were performed in a Tecnai G^2 F30 transmission electron microscope, equipped with X-ray energy-dispersive spectrometer (EDS) systems, operated at 300 kV. HAADF-STEM images were acquired using aberration-corrected scanning transmission electron microscope (Titan Cubed 60−300 kV microscope (FEI)). The microscope is fitted with a high-brightness field-emission gun (X-FEG), a monochromator, and double aberration (Cs) correctors from CEOS operating at 300 kV. The HAADF-STEM images were recorded with a convergence angle of 21.4 mrad and a collection angle of 50−250 mrad. The atom column positions were carried out by fitting them as 2D Gaussian peaks using Matlab software.[22,23]

DOI: 10.1021/acs.jpcc.8b10678
J. Phys. Chem. C 2019, 123, 2557−2564

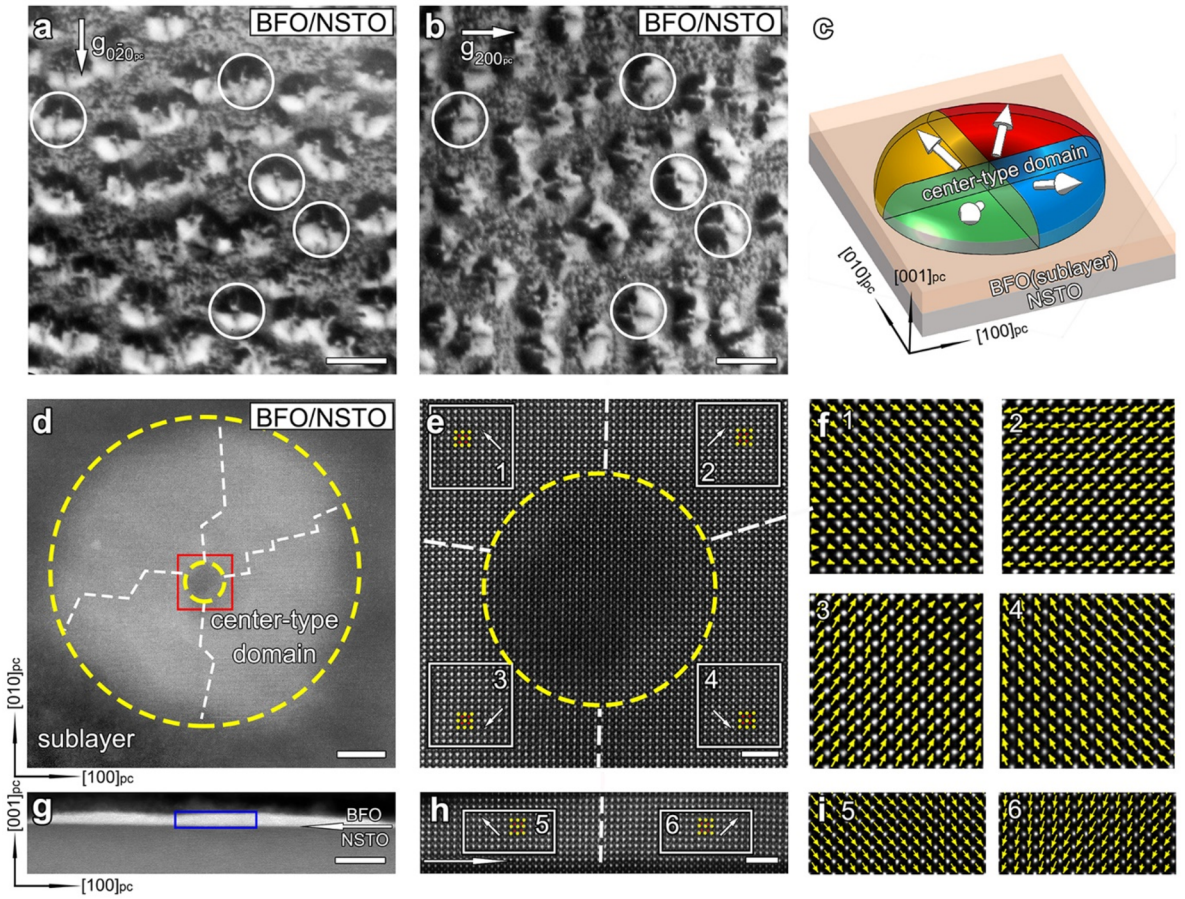

Figure 2. TEM and HAADF-STEM analysis on the domain configuration of BFO nanoislands on NSTO substrate. (a, b) Plane-view two-beam dark-field images of 6 nm BFO on NSTO (0.7 wt %) substrates taken by different reflections of $g = 0\bar{2}0_{pc}$ (a) and $g = 200_{pc}$ (b), respectively. The white circles marked some corresponding nanoislands in these two images. Scale bars in (a, b), 200 nm. (c) Schematic of domain configuration in these BFO nanoislands based on the analysis of both PFM and TEM characterization. Plane-view (d) and cross-sectional (g) HAADF images of single typical nanoisland in the film. Scale bar, 20 nm. (e) and (h) are atomically resolved HAADF images corresponding to the red square area in (d) and blue rectangle in (g), respectively. Scale bars in (e, h), 2 nm. The yellow and red solid circles denote the position of Bi^{3+} and Fe^{3+} columns; the white arrows indicate the direction of in-plane polarization component in each domain. (f) and (i) are superpositions of Fe^{3+} displacement vectors with enlarged atomic mappings of each numbered white square (rectangle) in (e) and (h), respectively. The white dashed lines in these images indicate 71° domain walls; the yellow dashed circles denote the boundary of the nanoisland.

2.4. Phase-Field Modeling. The computation model consists of a BFO film, above which a nanoisland is located. The height of nanoisland and the film thickness are both set as 3 nm. The in-plane size of the model is 300 × 300 nm^2. The diameter of nanoisland is about 150 nm. The surface of film and island is charged with the surface charge density (σ = ±0.25 C/m^2). The mechanical boundary condition compatible with the epitaxial film is applied in this model: The area far from the film−substrate interface is set in a uniform-strain state, while the top surface of film and nanoisland is in a stress-free state. For the electric boundary condition, the potential of the film bottom is constant, while the top surface is set in a state of a constant electric displacement. Detailed information on phase-field simulation can be found in the Supporting Information.

2.5. X-ray Photoelectron Spectroscopy and Valence Band Spectrum. The valence band spectrum was carried out on an ESCALAB250 Scientific instrument. A monochromatic X-ray source which provide Al kα X-rays ≈1486.6 eV with energy resolution of around 0.5 eV was employed, consisting of a high-power electron gun (15 kV, 150 W).

3. RESULTS AND DISCUSSION

3.1. Fabrication of $BiFeO_3$ Nanoislands. By using PLD method, self-assembled nanoislands of BFO were deposited on NSTO and FSTO substrates. The growth condition (such as substrate temperature, oxygen pressure, incident intensity, pulse repetition rate, etc.) is of great influence on the films (constitution, growth mechanism, thickness, etc.) in PLD. In our case, a high repetition of 10 Hz and a relatively high laser energy density of 2 $J{\cdot}cm^{-2}$ are chosen throughout the deposition in order to acquire BFO nanoislands. As a matter of fact, the growth regime tends to change under high repetition rate. That is because the time interval between two pulses decreases as the repetition rate is increased, which would ensure the rapidly nucleated small nuclei not spreading and growing fast to be stable. As a result, high density of nanoislands can be acquired.[24,25] Different doping levels of (001) oriented NSTO (0.1 and 0.7 wt %) and FSTO (0.005 and 0.05 wt %) substrates are used for further investigation of domain structures in BFO nanoislands and their formation mechanism.

3.2. Topography and PFM Measurements. First, PFM measurements are applied to investigate the morphology and

DOI: 10.1021/acs.jpcc.8b10678
J. Phys. Chem. C 2019, 123, 2557−2564

domain structures in these films. Figure 1a shows the topography of 6 nm (the height of nanoislands) BFO grown on (001) oriented NSTO (0.7 wt %) substrates. Vast amounts of BFO nanoislands are uniformly distributed on the substrate. In fact, the BFO film forms a two-layers feature with lots of BFO nanoislands shown as the bright contrast surrounded by a sublayer (about 3 nm in thickness) shown as the dark contrast in the image. The radii of these nanoislands are measured to be around 75 nm. Figure 1b and c are the topography and corresponding VPFM images of BFO nanoislands after writing an area of 3 × 3 μm^2 with a voltage of −10 V and then the inside 1.6 × 1.6 μm^2 with a voltage of +15 V. Since the negative voltage applied would switch to upward out-of-plane polarization in the film, the phase contrast indicates that the out-of-plane polarization in these nanoislands are pointing upward whereas that in the sublayer is pointing downward. Note that a larger positive voltage is needed to switch to downward polarization in the film. The asymmetric switchable characteristic is considered to be caused by the built-in potential due to Bi deficiency in the film.[26] (The Bi deficiency is discussed later in detail.) The out-of-plane polarization of the inner part in these nanoislands shows an opposite contrast which can be clearly seen in the enlarged VPFM image of the unpoled single nanoisland as the inset in Figure 1c. These nanoislands also appear as a dark center contrast in HAADF images shown in Figure S1a. We tend to believe that there is a void in the center of the nanoislands where no $BiFeO_3$ can be identified. EDS mappings of single nanoisland in Figure S1 confirm the lack of Bi and Fe elements. The strong signals of Sr, Ti, and O elements in Figure S1 also support that there may only exist substrates in the cores. We considered these atomic vacancies as the atomic interdiffusion formed "Kirkendall voids" during the deposition and the latter annealing procedure after deposition in the film due to the spontaneously formed dipole disclination in the core.[27,28]

The in-plane polarizations of these nanoislands have also been investigated. Figure 1d−f are LPFM images of the BFO film with anticlockwise sample rotation for 0° (d), 45° (e), and 90° (f). Upper right insets in (d)−(f) are topographies of the images. The cantilever in each case is also shown as the blue arrow. The horizontal directions are set to be $[100]_{pc}$ (the subscript "pc" denotes pseudo-cubic orientation) in these images for comparison. In Figure 1d, the lateral polarization of all these nanoislands appears a half-bright, half-dark feature. The contrast between left and right parts is clearly shown in the lower left inset as an enlarged LPFM image of single typical nanoisland. The domain wall is marked out with a white dashed line showing a zigzag-like feature. It was previously reported that the phase contrast in the LPFM corresponds to the in-plane polarization component perpendicular to the cantilever.[29] Based on this statement, we can reconstruct the in-plane polarization directions of these nanoislands by comparing the LPFM images at different sample rotation angles. In each image, the net polarization perpendicular to the cantilever is denoted by the white arrow. As we can see, the LPFM image with the sample rotation of 0° shows an opposite polarization component along $[100]_{pc}$ between the half left and right areas. Likewise, the half upper left and lower right part of the nanoislands show opposite polarization components along the $[1\bar{1}0]_{pc}$ direction, and the half up and down parts of the nanoislands show opposite polarization components along the $[010]_{pc}$ direction. The reconstruction of the in-plane polarization based on the analysis above shows that all of the nanoislands form an identical so-called center-type topological domain structure.[8]

3.3. TEM Characterizations of BFO Nanoislands. TEM and atomically resolved high-angle annular dark-field (HAADF) scanning transmission electron microscopy (STEM) imagings are used for further investigation of the domain structure in these nanoislands at atomic scale. Figure 2a and b are two-beam plane-view dark-field images in the same area of 6 nm BFO on NSTO (0.7 wt %) substrate taken by different reflections of $g = 0\bar{2}0_{pc}$ (a) and $g = 200_{pc}$ (b), respectively. The white circles marked out some corresponding nanoislands in these two images in which the four-quadrant domain configuration is unambiguous. In ferroelectric materials, the polarization vector (P_s) of bright contrast area in dark-field image satisfies $g \cdot P_s > 0$ under two-beam condition.[30] Thus, the direction of P_s can be determined. The top and bottom parts show a divert polarization direction along $[010]_{pc}$ in (a), and the left and right parts of the nanoislands show a divert polarization direction along the $[100]_{pc}$ direction in (b), which agree well with the LPFM in Figure 1. Considering that the out-of-plane polarization is consistent in the four domains, the domain walls formed between them in these BFO nanoislands are determined to be 71° tail-to-tail charged domain walls. Note that most of the domain walls are tortuous and show a zigzag-like domain wall feature, which is clearly revealed in Figure S2. Zigzag domain walls feature was also reported in previous studies in $BaTiO_3$ film[31,32] to minimize the electrostatic energy of neighboring domains. In this case, the zigzag-like domain walls will also help reduce the electrostatic energy in the nanoislands. HAADF-STEM imaging is applied for more refined investigation of the polarization distribution at atomic scale. Plane-view and cross-sectional HAADF images of one typical BFO nanoisland are shown in Figure 2d and g, respectively, from which the boundary of the nanoislands can be clearly seen. The "Kirkendall void" is marked by the small yellow dashed circle in Figure 2d in the center. Since the voids in the center contain no $BiFeO_3$, the atom columns in the atomically resolved HAADF images may correspond to NSTO substrates and thus show no polarization. Figure 2e is the atomically resolved HAADF image corresponding to the red square in Figure 2d. The yellow and red solid circles denote the position of Bi^{3+} and Fe^{3+} columns, in which the directions of the in-plane polarization components denoted by white arrows in each image (opposite to Fe^{3+} ion displacements) are obvious. The superposition of Fe^{3+} displacement vectors with enlarged atomic mapping of each numbered square is shown in Figure 2f. From this image, the in-plane polarization components of the four quadrants form a center-divergent arrangement. (The whole superposition of Fe^{3+} displacement vectors with atomic mapping (Figure 2e) is shown in Figure S3a, in which the 71° tail-to-tail charged domain walls can be clearly seen.) The cross-sectional atomically resolved HAADF image of the nanoislands has also been investigated and is shown in Figure 2h. The superposition of Fe^{3+} displacement vectors with enlarged atomic mapping of each numbered rectangle in Figure 2h is shown in Figure 2i. (The whole superposition of Fe^{3+} displacement vectors with atomic mapping (Figure 2h) is shown in Figure S3b.) Thus, the panorama of the domain structure in these nanoislands grown on NSTO substrate has been clarified. The four quadrant domains in these nanodomains form a center-divergent domain structure with upward polarization along the out-of-plane direction as

DOI: 10.1021/acs.jpcc.8b10678
J. Phys. Chem. C 2019, 123, 2557−2564

illustrated in Figure 2c. These four domains are separated by 71° tail-to-tail charged domain walls with zigzag-like feature which are verified by atomically resolved HAADF-STEM imaging. All of the white dashed lines in Figure 2 correspond to these 71° domain walls.

The domain configurations of the 6 nm BFO nanoislands grown on Fe:$SrTiO_3$ (FSTO) (0.05 wt %) (001) substrates have also been investigated using PFM, TEM, and HADDF-STEM imaging in order to explore the influence of substrate on the domain configuration of these nanoislands. The results are shown in Figures S4 and S5. Similarly, these nanoislands also appear as a four-quadrant center-divergent domain structure with 71° tail-to-tail charged domain walls resembling that grown on NSTO substrates, although the shape of these nanoislands is more irregular. The out-of-plane polarizations of both the nanoislands and sublayer are pointing upward. The results confirm that the donor doping and acceptor doping of the substrate would change the polarization distribution of the sublayer but not the center-type domains. More details are shown in the Supporting Information.

3.4. Manipulation of the Nanoislands. Topological domains are of vital importance for further utilization in nonvolatile memory devices, which would be in need of controllable preparation of such topological domains. In our case, the topological domains are center-type domains in the nanoislands. Since these BFO nanoislands grown on both NSTO and FSTO substrates display the same four-quadrant center-divergent domain structure and appear relevant to the metal doping, it is essential to learn the impact of doping level in substrates on the evolution of center domains. Figure 3a and b show the topography of BFO films deposited on NSTO substrates with different doping amounts. Figure 3c and d are their corresponding plane-view bright-field images taken by reflection of $g = 200_{pc}$. The doping amounts in the substrates are shown in the upper right corner of each image. By comparing Figure 3a and b (or c and d), we can infer that the density of nanoislands increases when the amount of doping increases, whereas the size of these nanoislands is not very sensitive to the amount of doping. The same goes for BFO nanoislands grown on FSTO substrates as shown in Figure S7.

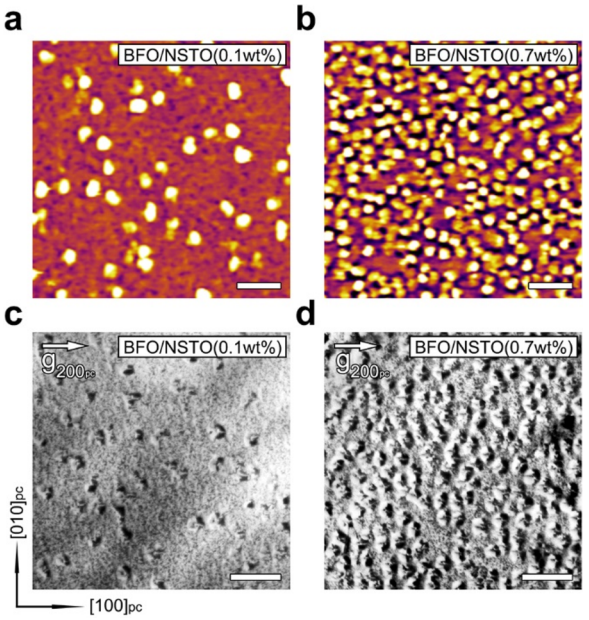

Figure 3. Influence of doping in substrates on center-type domains in BFO nanoislands. (a, b) Topographies of BFO films deposited on NSTO substrates with different doping amounts in these substrates. (c, d) Their corresponding plane-view bright-field images taken by reflection of $g = 200_{pc}$. All scale bars indicate 500 nm.

Besides, we also compared the BFO nanoislands with different thicknesses, which is shown in Figure S8. The diameter of these nanoislands shows an obvious increase when we increase the thickness of the film. Note that when the thickness reached 8 nm, the nanoislands would meet with its adjacent ones and coalesce.

3.5. Formation Mechanism of the Center-Type Domains. However, the formation mechanism of these nanoislands remains to be deeply investigated. It is noticed that similar center-type domain structures in BFO nanoislands have also been reported recently.[17,21] The formation mechanism of the center-type domain is ascribed to the surface charge accumulation. In order to understand the formation mechanism of the center-type domains in our nanoislands, phase-field simulations were used to systematically study the polarization distributions in the nanoislands. In our case, singular center-divergent domains are formed in all of the nanoislands with definite upward polarizations. Atomically resolved HAADF-STEM imaging revealed that the center-type domains are separated by four 71° charged domain walls with zigzag-like configurations. At first, a cylindrical nanodot model 150 nm in diameter and 3 nm in height was used for simulation. Considering that bismuth is volatile during the deposition, the Bi content in the grown film is smaller than the content in the source target.[33] Since the target we use is stoichiometric, Bi deficiency at the surface of these films is probably involved which would cause negative surface charges accumulation. Since the volatility of Fe is rather weak compared with that of Bi, the nanoislands are supposed to contain a tiny amount of Fe vacancies (except the void in the center where no $BiFeO_3$ can be identified). These Fe vacancies (if there are any) may also contribute to the negative charges accumulation at the surface. After the negative charge accumulation is set at the surface, the obtained domain structures are shown in Figure 4. It is noted that the out-of-plane polarization is pointing upward which is consistent with experiment results, while the in-plane polarization shows a center-convergent configuration (Figure 4c). This domain configuration is not the case in our work. A close observation of the nanoislands revealed that these spontaneously formed islands are more or less in a Gaussian shape and not a cylindrical shape.

After taking the shape of these nanoislands into consideration, we have redesigned our model so that the nanoisland is in a Gaussian shape, and the result is shown in Figure 5. To simulate the effect of surface charge, the surfaces of both the sublayer and the island are negatively charged with the surface charge density about 0.25 C/m^2, as shown in Figure 5b. Other technical details can be found in the Supporting Information. In this case, a divergent polarization distribution is found in the nanoisland, with the out-of-plane polarization pointing upward, as shown in Figure 5c. The simulation results perfectly reproduce the experimental ones, which indicates that the shape of nanoisland is a key factor to control the polarization distribution. Between the four divergent domains, there are actually charged 71° domain walls. It is also worthy to be noted that these charged domain walls form a zigzag-like configuration, which matches with the experiment results perfectly

DOI: 10.1021/acs.jpcc.8b10678
J. Phys. Chem. C 2019, 123, 2557−2564

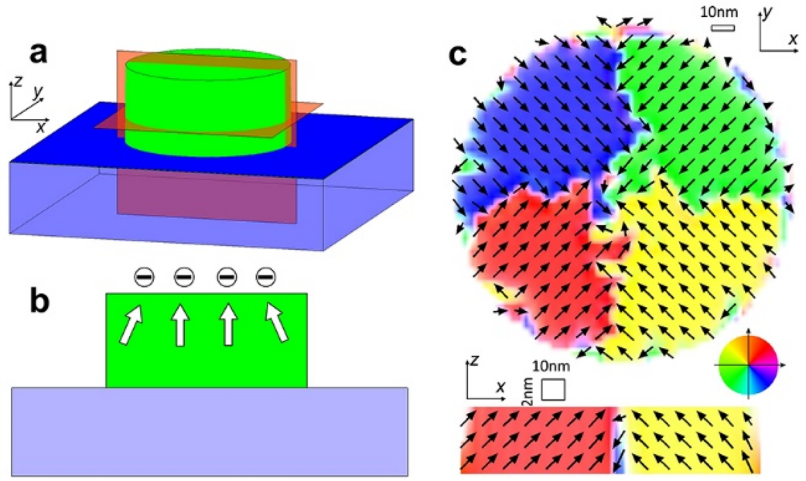

Figure 4. Phase-field simulation of a single BFO nanoisland with a cylindrical shape and negative surface charge. (a) Schematic diagram of the model with a 3 nm thick film and a 3 nm high nanoisland. (b) Schematic showing the distributions of negative surface charge and the resulting electric field (shown as the white arrows). (c) The polarization vector distributions of the nanoisland. The two figures in (c) correspond to the horizontal and vertical slices in (a), respectively.

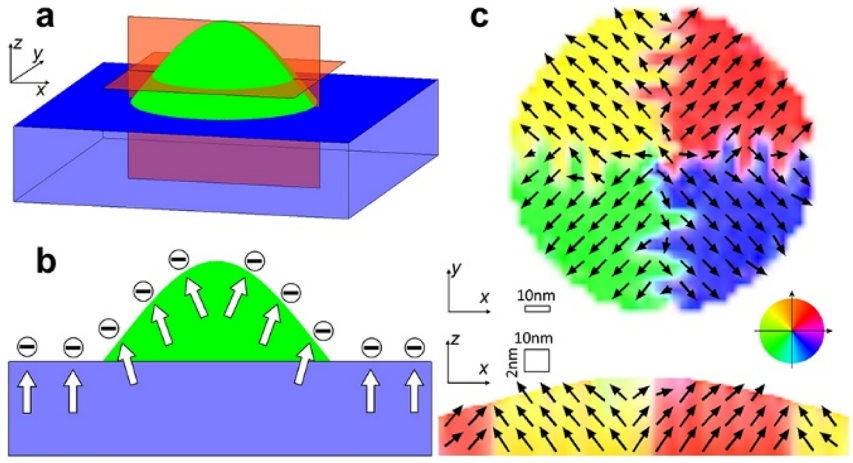

Figure 5. Phase-field simulation of a single BFO nanoisland with a Gaussian shape and negative surface charge. (a) Schematic diagram of the model with a 3 nm thick film and a 3 nm high nanoisland. (b) Schematic showing the distributions of negative surface charge and the resulting electric field (shown as the white arrows). (c) The polarization vector distributions of the nanoisland. The two figures in (c) correspond to the horizontal and vertical slices in (a), respectively.

and in turn confirms the authenticity and reliability of the phase-field simulation results.

To further understand the formation reason for this kind of center domain, the electric field distribution generated by the negative surface charge is also schematically simulated and is shown in Figure 5b. The electric field forms a divergent distribution in the nanoisland. However, the electric field forms a convergent distribution in the cylindrical shape model (Figure 4b). We can conclude that it is this kind of electric field distribution that drives the formation of center-divergent domains. To further demonstrate the effect of surface charge on the domain structure, the case of positive charge density is also considered, and the result is shown in Figure S9. It is found that the electric field generated by the surface charge forms a convergent distribution which results in center-convergent domains with the downward out-of-plane polarization. Summarizing these phase-field simulation results, it is obvious that both the shape and the surface charge have great impact on the domain pattern in the nanoislands. More specifically, the surface charge accumulation would take more effect on the out-of-plane polarization direction, whereas the shape of the nanoislands take more effect on the in-plane polarization distribution. That would explain why the nanoislands on both NSTO and FSTO substrates form the same center-divergent domains with upward polarization. It should be noted that the Bi and Fe deficiency would end up with a void in the core of nanoislands which may cause the fluctuation of charge distribution in the center, resulting in local polarization variation. This region, however, should be small compared with the sizes of nanoislands. Based on the results above, we believe that the local fluctuation of charge distribution in the core has negligible effect on the domain configuration in the whole nanoisland.

The center-type domains with adjustable polarization distributions hold great promise for next-generation nonvolatile memory devices, especially with manipulation of the size and density of the center-type domains. Howver, we also need to understand the reason for the size and density manipulation. The size of the nanoislands increases with thickness of the film which comes from the growth of the

DOI: 10.1021/acs.jpcc.8b10678
J. Phys. Chem. C 2019, 123, 2557−2564

nanoislands. The density of nanoislands increases with the increasing doping level of both Nb and Fe, which may result from the increment of surface charge density as the doping amount is increased. Taking NSTO as an example, niobium is a donor doping element, which would form a positively charged niobium atom fixed in the crystal.[34] During the deposition, the heated plasma which carries vapored materials formed in one pulse would travel to and be absorbed by the substrate surface, and then the successive pulses would carry more vapored matters to the surface and end up with the growth of the film. The positively charged center at the surface of NSTO would absorb vapored substances easily and thus form a BFO nanoisland after the deposition. If the Nb doping amount is increased, the positively charged center would also increase, and high density of nanoislands would then be generated. The same goes for BFO nanoislands grown on FSTO substrates. Under this circumstance, we can make use of both the film thickness and doping level in the substrates to manipulate the size and density of center-type domains and possibly acquire high-density nanoscale electronic devices.

4. CONCLUSIONS

In summary, self-assembled BFO nanoislands are deposited on NSTO and FSTO substrates by growth condition modulation. PFM, TEM, and atomically resolved HAADF-STEM imaging proved that these nanoislands form the same four-quadrant center-divergent domain structure. Four 71° charged domain walls mediating the center-type domains was first revealed at an atomic scale. In a combination of phase-field modeling, it is proposed that the formation mechanism of such domain structure lies in negative surface charge accumulation due to Bi deficiency at the surface and the Gaussian shape of the nanoislands. Without using nanoporous anodic alumina template, our method provides a rather economical method to acquire self-assembled nanoscale devices. Moreover, the size and density of these center-type domains can be manipulated easily by the film thickness and the doping amount in these substrates, offering a promising pathway to acquire high-density data storage for nonvolatile memories.

■ ASSOCIATED CONTENT

Supporting Information

The Supporting Information is available free of charge on the ACS Publications website at DOI: 10.1021/acs.jpcc.8b10678.

Details of phase-field simulations; EDS elemental mapping of a single BFO nanoisland; zigzag-shaped domain walls; details of the polarization distribution in BFO nanoislands; domain configuration and polarization distribution of BFO nanoislands grown on FSTO substrates; the influence of substrates on the polarization of the sublayer; the influence of doping amount and thickness on the BFO nanoislands; phase-field simulation of BFO nanoisland with positive surface charge (PDF)

■ AUTHOR INFORMATION

Corresponding Authors

*E-mail: ylzhu@imr.ac.cn.
*E-mail: xlma@imr.ac.cn.

ORCID

Yin-Lian Zhu: 0000-0002-0356-3306

Author Contributions

[⊥]X.-L.M. and Y.-L.Z. conceived the project of structural and functional characterization in oxides by using PFM and Cs-corrected scanning transmission electron microscopy. M.-J.H., Y.-L.Z., and X.-L.M. designed the experiments. M.-J.H. performed the films growth, PFM, STEM, and XPS measurements and analyzed the data. Y.-J.W. carried out phase-field simulations. Y.-L.T., J.-Y.M., W.-R.G., M.-J.Z., Y.-P.F., and N.-B.Z. participated in the thin films growth, PFM, and STEM imaging. All authors contributed to the discussions and manuscript preparation. M.-J.H. and Y.-J.W.contributed equally to this work.

Notes

The authors declare no competing financial interest.

■ ACKNOWLEDGMENTS

This work is supported by the National Natural Science Foundation of China (No. 51571197, 51501194 and 51671194), National Basic Research Program of China (2014CB921002), and the Key Research Program of Frontier Sciences CAS (QYZDJ-SSW-JSC010). Y.-L.T. acknowledges the IMR SYNL-T.S. Kê Research Fellowship and the Youth Innovation Promotion Association CAS (No. 2016177). We are grateful to Mr. B. Wu and Mr. L. X. Yang of this lab for their technical support on the Titan platform of G2 60-300 kV aberration-corrected scanning transmission electron microscope.

■ REFERENCES

(1) Mermin, N. D. The Topological Theory of Defects in Ordered Media. *Rev. Mod. Phys.* **1979**, *51*, 591−648.

(2) Seidel, J.; Vasudevan, R. K.; Valanoor, N. Topological Structures in Multiferroics - Domain Walls, Skyrmions and Vortices. *Adv. Electron. Mater.* **2016**, *2*, 1500292.

(3) Fu, H.; Bellaiche, L. Ferroelectricity in Barium Titanate Quantum Dots and Wires. *Phys. Rev. Lett.* **2003**, *91*, 257601.

(4) Naumov, I. I.; Bellaiche, L.; Fu, H. Unusual Phase Transitions in Ferroelectric Nanodisks and Nanorods. *Nature* **2004**, *432*, 737−740.

(5) Gruverman, A.; Wu, D.; Fan, H. J.; Vrejoiu, I.; Alexe, M.; Harrison, R. J.; Scott, J. F. Vortex Ferroelectric Domains. *J. Phys.: Condens. Matter* **2008**, *20*, 342201.

(6) Rodriguez, B. J.; Gao, X. S.; Liu, L. F.; Lee, W.; Naumov, I. I.; Bratkovsky, A. M.; Hesse, D.; Alexe, M. Vortex Polarization States in Nanoscale Ferroelectric Arrays. *Nano Lett.* **2009**, *9*, 1127−1131.

(7) Balke, N.; Choudhury, S.; Jesse, S.; Huijben, M.; Chu, Y. H.; Baddorf, A. P.; Chen, L. Q.; Ramesh, R.; Kalinin, S. V. Deterministic Control of Ferroelastic Switching in Multiferroic Materials. *Nat. Nanotechnol.* **2009**, *4*, 868−875.

(8) Vasudevan, R. K.; Chen, Y. C.; Tai, H. H.; Balke, N.; Wu, P. P.; Bhattacharya, S.; Chen, L. Q.; Chu, Y. H.; Lin, I. N.; Kalinin, S. V.; et al. Exploring Topological Defects in Epitaxial $BiFeO_3$ Thin Films. *ACS Nano* **2011**, *5*, 879−887.

(9) Balke, N.; Winchester, B.; Ren, W.; Chu, Y. H.; Morozovska, A. N.; Eliseev, E. A.; Huijben, M.; Vasudevan, R. K.; Maksymovych, P.; Britson, J.; et al. Enhanced Electric Conductivity at Ferroelectric Vortex Cores in $BiFeO_3$. *Nat. Phys.* **2012**, *8*, 81−88.

(10) Tang, Y. L.; Zhu, Y. L.; Ma, X. L.; Borisevich, A. Y.; Morozovska, A. N.; Eliseev, E. A.; Wang, W. Y.; Wang, Y. J.; Xu, Y. B.; Zhang, Z. D.; et al. Observation of a Periodic Array of Flux-Closure Quadrants in Strained Ferroelectric $PbTiO_3$ Films. *Science* **2015**, *348*, 547−551.

(11) Yadav, A. K.; Nelson, C. T.; Hsu, S. L.; Hong, Z.; Clarkson, J. D.; Schlepütz, C. M.; Damodaran, A. R.; Shafer, P.; Arenholz, E.; Dedon, L. R.; et al. Observation of Polar Vortices in Oxide Superlattices. *Nature* **2016**, *530*, 198−201.

DOI: 10.1021/acs.jpcc.8b10678
J. Phys. Chem. C 2019, 123, 2557−2564

(12) Damodaran, A. R.; Clarkson, J. D.; Hong, Z.; Liu, H.; Yadav, A. K.; Nelson, C. T.; Hsu, S. L.; McCarter, M. R.; Park, K. D.; Kravtsov, V.; et al. Phase Coexistence and Electric-Field Control of Toroidal Order in Oxide Superlattices. *Nat. Mater.* **2017**, *16*, 1003−1009.
(13) Hong, Z.; Damodaran, A. R.; Xue, F.; Hsu, S. L.; Britson, J.; Yadav, A. K.; Nelson, C. T.; Wang, J.; Scott, J. F.; Martin, L. W.; et al. Stability of Polar Vortex Lattice in Ferroelectric Superlattices. *Nano Lett.* **2017**, *17*, 2246−2252.
(14) Van Lich, L. V.; Shimada, T.; Wang, J.; Dinh, V. H.; Bui, T. Q.; Kitamura, T. Switching the Chirality of a Ferroelectric Vortex in Designed Nanostructures by a Homogeneous Electric Field. *Phys. Rev. B: Condens. Matter Mater. Phys.* **2017**, *96*, 134119.
(15) Shafer, P.; Garcia-Fernandez, P.; Aguado-Puente, P.; Damodaran, A. R.; Yadav, A. K.; Nelson, C. T.; Hsu, S. L.; Wojdel, J. C.; Iniguez, J.; Martin, L. W.; et al. Emergent Chirality in the Electric Polarization Texture of Titanate Superlattices. *Proc. Natl. Acad. Sci. U. S. A.* **2018**, *115*, 915−920.
(16) Chen, Y. C.; Wang, G. F.; Tai, H. H.; Chen, J. W.; Huang, Y. C.; Yang, J. C.; Chu, Y. H. Non-Volatile Domain Nucleation and Growth in Multiferroic $BiFeO_3$ Films. *Nanotechnology* **2011**, *22*, 254030.
(17) Li, Z.; Wang, Y. J.; Tian, G.; Li, P. L.; Zhao, L.; Zhang, F. Y.; Yao, J. X.; Fan, H.; Song, X.; Chen, D. Y.; et al. High-Density Array of Ferroelectric Nanodots with Robust and Reversibly Switchable Topological Domain States. *Sci. Adv.* **2017**, *3*, e1700919.
(18) Zhang, Q.; Xie, L.; Liu, G.; Prokhorenko, S.; Nahas, Y.; Pan, X.; Bellaiche, L.; Gruverman, A.; Valanoor, N. Nanoscale Bubble Domains and Topological Transitions in Ultrathin Ferroelectric Films. *Adv. Mater.* **2017**, *29*, 1702375.
(19) Li, L.; Cheng, X.; Jokisaari, J. R.; Gao, P.; Britson, J.; Adamo, C.; Heikes, C.; Schlom, D. G.; Chen, L. Q.; Pan, X. Defect-Induced Hedgehog Polarization States in Multiferroics. *Phys. Rev. Lett.* **2018**, *120*, 137602.
(20) Lu, L.; Nahas, Y.; Liu, M.; Du, H.; Jiang, Z.; Ren, S.; Wang, D.; Jin, L.; Prokhorenko, S.; Jia, C. L.; et al. Topological Defects with Distinct Dipole Configurations in $PbTiO_3/SrTiO_3$ Multilayer Films. *Phys. Rev. Lett.* **2018**, *120*, 177601.
(21) Ma, J.; Ma, J.; Zhang, Q.; Peng, R.; Wang, J.; Liu, C.; Wang, M.; Li, N.; Chen, M.; Cheng, X.; et al. Controllable Conductive Readout in Self-Assembled, Topologically Confined Ferroelectric Domain Walls. *Nat. Nanotechnol.* **2018**, *13*, 947−952.
(22) Anthony, S. M.; Granick, S. Image Analysis with Rapid and Accurate Two-Dimensional Gaussian Fitting. *Langmuir* **2009**, *25*, 8152−8160.
(23) Jia, C. L.; Nagarajan, V.; He, J. Q.; Houben, L.; Zhao, T.; Ramesh, R.; Urban, K.; Waser, R. Unit-Cell Scale Mapping of Ferroelectricity and Tetragonality in Epitaxial Ultrathin Ferroelectric Films. *Nat. Mater.* **2007**, *6*, 64−69.
(24) Chang, C. C.; Wu, X. D.; Ramesh, R.; Xi, X. X.; Ravi, T. S.; Venkatesan, T.; Hwang, D. M.; Muenchausen, R. E.; Foltyn, S.; Nogar, N. S. Origin of Surface Roughness for c-axis Oriented Y-Ba-Cu-O Superconducting Films. *Appl. Phys. Lett.* **1990**, *57*, 1814−1816.
(25) Develos, K. D.; Kusunoki, M.; Mukaida, M.; Ohshima, S. Effect of Deposition Rate on the Surface Morphology of CeO_2 Films Deposited by Pulsed Laser Deposition. *Phys. C* **1999**, *320*, 21−30.
(26) Jesse, S.; Lee, H. N.; Kalinin, S. V. Quantitative Mapping of Switching Behavior in Piezoresponse Force Microscopy. *Rev. Sci. Instrum.* **2006**, *77*, 073702.
(27) Maurice, V.; Despert, G.; Zanna, S.; Bacos, M. P.; Marcus, P. Self-Assembling of Atomic Vacancies at an Oxide/Intermetallic Alloy Interface. *Nat. Mater.* **2004**, *3*, 687−691.
(28) Crosby, L.; Enterkin, J.; Rabuffetti, F.; Poeppelmeier, K.; Marks, L. Wulff Shape of Strontium Titanate Nanocuboids. *Surf. Sci.* **2015**, *632*, L22−L25.
(29) Ganpule, C. S.; Nagarajan, V.; Hill, B. K.; Roytburd, A. L.; Williams, E. D.; Ramesh, R.; Alpay, S. P.; Roelofs, A.; Waser, R.; Eng, L. M. Imaging Three-Dimensional Polarization in Epitaxial Polydomain Ferroelectric Thin Films. *J. Appl. Phys.* **2002**, *91*, 1477.
(30) Asada, T.; Koyama, Y. Coexistence of Ferroelectricity and Antiferroelectricity in Lead Zirconate Titanate. *Phys. Rev. B: Condens. Matter Mater. Phys.* **2004**, *70*, 104105.
(31) Yakunin, S. I.; Shakmano, V. V.; Spivak, G. V.; Vasil'eva, N. V. Microstructure of Domains and Domain Boundaries of $BaTiO_3$ Single Crystalline Films. *Fiz. Tverd. Tela* **1972**, *14*, 373.
(32) Lines, M. E.; Glass, A. M. *Principles and Applications of Ferroelectrics and Related Materials*; Oxford University Press: Oxford, U.K., 1977.
(33) Tsurumaki, A.; Yamada, H.; Sawa, A. Impact of Bi Deficiencies on Ferroelectric Resistive Switching haracteristics Observed at p-Type Schottky-Like $Pt/Bi_{1-\delta}FeO_3$ Interfaces. *Adv. Funct. Mater.* **2012**, *22*, 1040−1047.
(34) Donald, A. N. *Semiconductor Physics and Devices:Basic Principles*; Publishing House of Electronics Industry: Beijing, China, 2011.

DOI: 10.1021/acs.jpcc.8b10678
J. Phys. Chem. C 2019, 123, 2557−2564